

# Monitoring and Modeling Lateral Transport through a Large In Situ Chamber

James L. Starr, Ali M. Sadeghi,\* and Yakov A. Pachepsky

## ABSTRACT

Accurate characterization of lateral transport components is an important step toward a more quantitative assessment of the fate and transport of nutrients and the functionality of riparian/wetland systems. Our specific objectives were: (i) to design an in situ chamber for studying lateral flow under shallow watertable and riparian zone conditions; (ii) to monitor predominantly horizontal transport of non-conservative ( $\text{NO}_3$ ) and conservative (Br) tracers in shallow saturated zone of the soil monolith; and (iii) to obtain reaction and transport parameters, and additional insights about the flow and transport inside the soil monolith. HYDRUS-2D model was used to simulate flow and transport of Br and  $\text{NO}_3$ , and to evaluate the applicability of this model to the observed flow and transport. Advective-dispersive equation (ADE) and mobile-immobile zone model (MIM) options were tested using the Br data. The breakthrough curves (BTCs) of  $\text{NO}_3$  and Br were similar while the concentrations rose, then became distinctly different with  $\text{NO}_3$  concentrations decreasing much faster. The calibrated denitrification rate of  $0.713 \pm 0.211 \text{ d}^{-1}$  was about an order and a half of magnitude larger in the loam layer (25–35 cm) than in the overlying sandy loam layer (0–25 cm) and in the sandy clay loam layer (35–65 cm) below. Up to 60% of the introduced  $\text{NO}_3$  was lost to denitrification. The methodology presented here allowed the in situ estimation reaction and transport needed for modeling; and it showed a potential to provide detailed information critical for the interpretation of the modeling outcomes performed at field and watershed levels.

THE EFFECTIVENESS of riparian areas to reduce nitrate contaminated shallow groundwater is controlled by many factors, including soil hydraulic properties and flow paths, denitrification rates, and plant uptake (Angier et al., 2002; Maître et al., 2003; Gilliam, 1994). Lateral subsurface flow from fertilized agricultural lands to and within riparian systems is a major mechanism for moving nitrates and other agrochemicals to ground- and surface-water bodies. Characterization of this transport component is an important first step toward quantitative assessment of the fate and transport of nutrients and better understanding of the functionality of the riparian/wetland systems. Furthermore, models are currently being developed to assess both the effectiveness of vegetative buffers/filters such as VFSSMOD (Vegetative Filter Strip Model) (Muñoz-Carpena et al., 1999) and the functionality of the riparian/wetland such as Riparian Ecosystem Management Model (REMM, Lowrance et al., 2000) in controlling pollutants from agricultural fields. The successful application and validation of these models, how-

ever, depend on the validity and best estimation of key hydrological as well as nutrient fate and transport parameters.

Several in situ methods have been used to assess lateral flow hydraulics and reactive properties of soils and ecosystems, each with advantages and disadvantages. The fate of  $\text{NO}_3\text{-N}$  in shallow groundwater is commonly estimated indirectly from changes in saturated zone concentrations along transects of slotted wells (Angier et al., 2002; Bosch et al., 1996; Jordan et al., 1993; Maître et al., 2003; Vellidis et al., 2003). Slotted wells have also been used in forced gradient cluster-well arrangements to assess in situ movement and losses of  $\text{NO}_3\text{-N}$  in shallow, laterally flowing groundwater (Starr et al., 1996; Bragan et al., 1997). In dual-tracer studies (e.g., Br and  $\text{NO}_3$ ), these techniques work quite well in shallow groundwater investigations to estimate in situ denitrification rates. However, the placement of the slotted wells may or may not be along the primary flow paths of water and solutes (Parkin et al., 1988; Hamilton et al., 1993), leading to large uncertainties for mass balances and estimated soil hydraulic parameters.

Other in situ approaches have used isolated soil blocks to obtain both horizontal and vertical flow parameters. For example, Day et al. (1998) excavated and instrumented a 3.38- $\text{m}^3$  soil block (at a footslope position underlain by a fragipan horizon) to obtain soil hydraulic parameters. A smaller (0.045  $\text{m}^3$ ), portable version of the in situ block method was developed and tested by Mendoza and Steenhuis (2002) to characterize subsurface flow on steep hill slopes. Although, these soil block methods have proven to be useful in many soil conditions, a primary disadvantage is the difficulty in their use in shallow water tables as commonly occurs in riparian zones.

Sadeghi and Starr (1992) designed a laboratory chamber to study and model lateral flow of water and solute transport under saturated conditions. In their chamber the inlet and outlet ports were arranged on a  $5 \times 5 \text{ cm}$  grid on both end walls that enabled them to maintain a nearly constant lateral hydraulic gradient and flow rate through the chamber, with simultaneous sampling from all the outlet ports. Their experimental approach worked reasonably well in the laboratory, and provided results that may lead to an effective method under field conditions. This paper explains the extension of that experimental approach to monitor lateral flow through a complex heterogeneous undisturbed soil monolith, that is, not a uniformly packed sand chamber. For this study, an in situ soil block was enclosed on four sides by an open-ended stainless steel chamber (SSC). This

J.L. Starr and A.M. Sadeghi, USDA-ARS Environmental Quality Lab., Bldg. 007, 10300 Baltimore Ave., Beltsville, MD 20705; Ya. A. Pachepsky, USDA-ARS Environmental Microbial Safety Lab., Beltsville, MD 20705. Received 7 May 2004. \*Corresponding author (sadeghia@ba.ars.usda.gov).

Published in Soil Sci. Soc. Am. J. 69:1871–1880 (2005).

Soil Physics

doi:10.2136/sssaj2004.0162

© Soil Science Society of America

677 S. Segoe Rd., Madison, WI 53711 USA

**Abbreviations:** ADE, advective-dispersive equation; BTC, breakthrough curve; CV, coefficient of variation;  $D_L$ , longitudinal dispersivity;  $D_T$ , transversal dispersivity;  $K_s$ , field saturated hydraulic conductivity; MIM, mobile-immobile zone model; REMM, Riparian ecosystem management model; SSC, stainless steel chamber.

field adaptation allows quantitative lateral flow examination of water and solute fluxes through an isolated section of a soil profile within a riparian area. Our goal was to understand and characterize the reaction (denitrification) and transport (hydraulics) in the shallow groundwater of a riparian zone soil. Specific objectives were to: (i) design an in situ chamber for studying lateral flow under shallow water-table and riparian zone conditions; (ii) to compare predominantly horizontal transport of nonconservative ( $\text{NO}_3$ ) and conservative (Br) tracers in shallow unsaturated zone, and (iii) to simulate transport of Br and  $\text{NO}_3$  with HYDRUS-2D (Simunek et al., 1999) to obtain reaction and transport parameters and additional insights about flow and transport inside the chamber.

## MATERIALS AND METHODS

### Site Conditions

This study was conducted on a Beltsville, Fallsington sandy loam (Typic Ochraquults, soil, with a slowly permeable sandy clay loam at the lower depths) at the Beltsville Agricultural Research Center, Beltsville, MD. The Beltsville series consists of moderately well drained soils with a compact fragipan subsoil. The experimental site was positioned near the bottom of a 5% landscape slope, with perennial long-term grass vegetation, mainly Tall Fescue (*Festuca elatior* L.). This site was immediately adjacent to a forested, intermittent first order stream, and located about 10 m downslope from the forced gradient cluster-well experiment reported by Starr et al. (1996). Soil profile data at this adjacent experimental site is presented in Table 1 (Starr et al., 1996). The clay content of the soil profile increased from 8.5% in the surface 15 cm to ~40% starting at the 65-cm depth (Table 1), resulting in a shift of USDA textural classification from sandy loam to sandy clay loam between 25- and 65-cm soil depths. The clay loam soil horizon, starting at 65 cm, contained ~50% gray mottling, indicating that the subsoil was anaerobic for substantial periods of time each year. Field saturated vertical hydraulic conductivities ( $K_s$ ) were measured at approximately the middle of each soil horizon (15-, 40-, 70-, and 100-cm depths) with a Guelph Permeameter (Reynolds and Elrick, 1985).

Coincident with increasing clay content with soil depth (Table 1), field-saturated hydraulic conductivity ( $K_s$ ) decreased by an order of magnitude between the 20- and 70-cm depths

(from 44 to 3.4  $\text{cm d}^{-1}$ ), and another order of magnitude from 70- to 110-cm depths (from 3.4- to 0.14  $\text{cm d}^{-1}$ ). This magnitude of change in  $K_s$  with depth made it possible to create a temporary phreatic lateral flow condition above the “confining” layer as commonly occurs under intermittent wetland/riparian conditions.

Soil temperature was not recorded, but other climatic data such as typical late summer daily air temperature during this experiment was recorded at a nearby weather station, with daily maximum and minimum averages of 28.9 and 16.8°C, respectively. There was no rainfall during the experiment.

### Field Installation

A 0.9 by 0.9 by 1.2 m open-ended SSC, with 3.2-mm wall thickness was lowered over an undisturbed block of soil that was precut to slightly larger dimensions. The bottom edges of the four walls were sharpened and tapered outward to shave the edges of the soil monolith as the SSC was lowered, providing tight contact between the soil and all four chamber walls. Galvanized sheet metal was used to create: human-access-wells at the inlet and outlet ends of the SSC (Fig. 1, #1); and space for gravel-filled chambers on two sides (#6a). All four galvanized sheet-metal chambers were bolted to the SSC corners. Five-centimeter diameter slotted well tubes (#5) were placed in the two side chambers just before filling these chambers with gravel. Float-valves were placed in these slotted tubes to maintain the desired water pressure head around the base of the SSC.

Before placing the SSC in the ground, inlet, and outlet port holes (#10) were drilled on a 10- by 10-cm grid, starting 5 cm from the outside edges, and stainless steel tubes (6.35-mm i.d.) were silver-soldered into the holes. After installing the SSC, fine-sand inlet and outlet porous plates (#8) were created in place to facilitate water and solute distribution from the grid of inlet ports to the two-dimensional soil face, and from the two-dimensional outlet soil face to the grid of outlet ports. The “end-plates” were created by carefully excavating a rectangular slice of soil next to the inlet and outlet walls ( $\sim 0.025 \times 0.90 \times 0.7$  m), using a specially designed tool, and then hand packing fine-sand in the space in 5-cm incremental layers.

To visually check the status of the water pressure in the soil surrounding the base of the SSC, clear acrylic standpipes were positioned in the floors of the two access wells (#4) just before pouring a gravel base in the two access wells (#6b). Concrete floors (#7) were then poured on the gravel base of the inlet and outlet chambers, and the concrete surface subsequently sealed with a marine paint/sealer to prevent leakage due to the hydrostatic head that was maintained below the concrete floor.

The water table in and around the SSC was maintained at the desired depth through float-valve controlled water lines placed in the slotted wells (#5). Water pressure in the gravel below the concrete floors was equilibrated with that in the side chambers by siphon tubes connecting #4 and #5, represented by the dashed lines in Fig. 1. During experimental runs, water (5 mM  $\text{CaSO}_4$ ) or tracer solution (same ionic strength, balanced with  $\text{CaSO}_4$ ) flowed by gravity from the storage reservoirs through buried nylon tubing (#2a) to a float-valve (#2b) controlled inlet manifold (#2), providing a constant water pressure head at the inlet face. The inlet manifold (#2) had a concave interior top connected to an air-bleed valve. Plastic tubing connected the ports at the bottom of the inlet manifold (#2) to the inlet ports on the SSC. The inlet solution was maintained at a near-constant temperature by delivery from 500-L storage reservoirs, placed inside an insulated mini-shed, through a 6.4-mm i.d. plastic tubing that was buried 1-m below the soil surface.

**Table 1. Soil profile characteristics.**<sup>†</sup>

Depth cm	Bulk density $\text{Mg m}^{-3}$	Particle-size distribution		Textural class <sup>‡</sup>	$K_s$ $\text{cm d}^{-1}$
		Sand	Clay		
		%			
0–15	1.17 (0.03)	62.2 (0.8)	8.7 (0.4)	SL	–
15–25	1.55 (0.03)	58.8 (0.9)	18.2 (2.9)	SL	44 (16)
25–35	1.61 (0.03)	44.1 (1.7)	25.2 (1.8)	L	–
35–45	1.61 (0.02)	44.9 (4.1)	27.0 (2.5)	SCL	14 (9)
45–55	1.72 (0.07)	48.1 (3.9)	25.7 (2.9)	SCL	–
55–65	1.62 (0.08)	48.2 (10.9)	31.9 (7.5)	SCL	–
65–75	1.62 (0.04)	35.8 (12.7)	39.7 (7.6)	CL	3.4 (0.9)
75–90	1.59 (0.01)	32.1 (9.5)	40.1 (6.3)	CL	–
90–100	1.62 (0.01)	38.7 (7.0)	36.9 (4.6)	CL	–
100–110	–	–	–	–	0.14 (0.1)

<sup>†</sup> Adapted from Starr et al. (1996), sampling area about 10 m from this lateral flow soil monolith.

<sup>‡</sup> SL = sandy loam, L = loam, SCL = sandy clay loam, CL = clay loam.

<sup>§</sup> Field-saturated vertical hydraulic conductivities (mean, [SE],  $n = 9$ ), measured with a Guelph Permeameter.

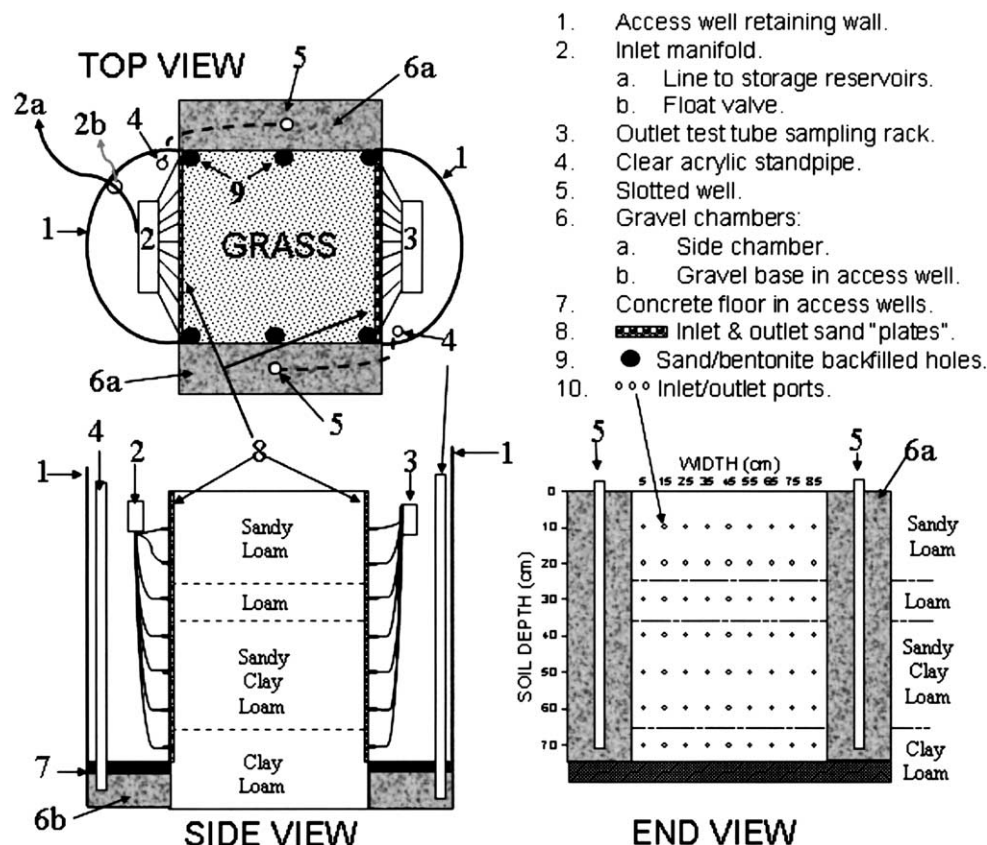


Fig. 1. Schematic of the in situ stainless steel chamber (0.9 by 0.9 by 1.2 m) layout and instrumentation for water table control, and the water inlet and outlet system.

Nylon tubing (3.2 mm o.d.) inserted through rubber serum stoppers connected the outlet ports of the SSC (#10) to a rack of test tubes (#3). The sampling apparatus (#3) consisted of a horizontal test tube holding tray, positioned such that all the tube outlets dripped from the same height relative to the SSC, and just above the rack of test tubes. The adjustable height sampling plate enabled precise water table control at the SSC outlet. After the first test-flow experiment, a sand-bentonite mix was placed in six soil-core holes (0.025-m diameter  $\times$  0.7-m deep) at the four corners and at the mid-points along the gravel-chamber walls (#9) to minimize by-pass flow along the walls.

### Flow Experiments

Water and tracer flow studies were conducted at constant inlet and outlet water pressure heads. The inlet water pressure was controlled by a float valve (Fig. 1, #2b), and positioned at a soil depth of 0.10 m (Row 1, Fig. 1, #10). The outlet water pressure head was maintained at a soil depth of 0.23 m (3 cm below outlet Row 2), that is, the height of the outlet drip line (described above). This resulted in a 14% pressure head gradient ( $\Delta h/\Delta x$ ) across the SSC. Both non-tracer and tracer inlet solutions were maintained at the same ionic strength (20). The non-tracer solution was a 5 mM  $\text{CaSO}_4$  solution; and the tracer solution contained 3 mM  $\text{Ca}(\text{NO}_3)_2$ , 1 mM KBr, and 2.5 mM  $\text{CaSO}_4$ . The  $\text{Ca}^{+2}$  concentration increased with the tracer solution only from 5.0 to 5.5 mM, plus the added 1 mM  $\text{K}^{+1}$ , thus little cationic effects on soil structure and water movement was expected with the changes to and from the tracer pulse. After establishing the constant gradient water flow, the tracer pulse was initiated by abruptly switching the inlet source from water to tracer solution, followed by quickly flushing

the entire line and inlet manifold with the tracer solution, and recording the initial time ( $t_0$ ). At the end of the 1.08-d tracer pulse, the inlet line was switched back to the 5 mM  $\text{CaSO}_4$  water and the end time of the pulse recorded. Samples were collected from each port at the outlet plate three to four times a day until most of the BTC was past. (Data presented here are for 5.5 d.) Bulk samples were collected between these sampling times by channeling the outlet flow to a large carboy. The starting and ending times were recorded at each sampling, and the sample volumes recorded by weight. Samples were either analyzed immediately, or stored at about 4°C and analyzed within 3 d. Bromide analysis was conducted with a Corning Specific Ion Bromide Electrode<sup>1</sup> and a portable Corning meter (Corning, Corning, NY). Nitrate concentrations were analyzed with an Alpkem Rapid Flow Analyzer (Alpkem, Corp., Clackamas, OR) using standard cadmium column reduction colorimetric analysis.

### Flow and Transport Simulations

We used HYDRUS-2D (Simunek et al., 1999) to simulate water flow and tracer transport in this experiment. The purpose of the simulations was to obtain additional insights about the flow and transport inside the soil monolith. The HYDRUS-2D code can simulate two-dimensional water, heat, and multiple solute transports in variably saturated porous media. We used the features of the code that allowed us to numerically solve the Richards' equation for saturated-unsaturated water flow

<sup>1</sup> Mention of trade names or commercial products in this article is solely for the purpose of providing specific information and does not imply recommendation or endorsement by the U.S. Department of Agriculture or an endorsement over other similar products.



and the convection-dispersion equation for solute transport. HYDRUS-2D includes a version of Marquardt–Levenberg algorithm that we used to calibrate the model. Hydraulic parameters were estimated with the Rosetta software, which is built into the HYDRUS-2D code.

We considered the two-dimensional flow in the vertical plane perpendicular to the chamber inlet/outlet. The flow domain was rectangular and was set to encompass the entire soil block. The bottom boundary was considered impermeable. Of course this is not a totally correct assumption since the chamber bottom was open to the low  $K_{fs}$  clay loam soil. However this assumption is essentially correct for these experimental conditions (imposed water table from below [Fig. 1]), as the data will show. The top boundary was simulated with atmospheric boundary conditions. The vegetation stand effect on water and solute transport was simulated using the Feddes root water uptake option in HYDRUS-2D with default parameters for grass (Simunek et al., 1999) with 30-cm root depth. Daily potential evapotranspiration values were calculated using the Hargreaves and Samani (1985) method, which uses max-min air temperature and solar radiation. Daily values were down-scaled into hourly values as described in Timlin et al. (2002). The mean values of water flux and flux-averaged breakthrough concentrations for each row (across nine outlets for each row) were simulated with a single slot positioned at the height of the outlet rows and having the same area as the total area associated with each outlet row (900 cm<sup>2</sup>). The constant head boundary conditions were set at the inlet and outlet rows for water flow according to the adjustable height outlet boundary plate (Fig. 1, #3) and the float-valve control at the inlet manifold (Fig. 1, #2b). The outlet ports at the second row were set as a HYDRUS-2D seepage-face boundary condition. The inlet boundary condition for the solute transport was set to a 1.08-d tracer pulse. Default numerical solution settings were used in HYDRUS-2D. The Crank-Nicholson method was used in the numerical solution. The van Genuchten water retention model and van Genuchten-Mualem hydraulic conductivity model were used (van Genuchten, 1980).

The soil within the chamber was considered to have four distinct layers (Fig. 1). The bottom boundaries of the layers were originally set at 25, 35, and 65 cm according to the soil profile observations (Table 1). For modeling purposes, the top of the clay loam layer was moved to 45-cm to cover the fifth outlet row because there was essentially no flow from that row. The sand plates at the inlet and outlet were simulated as a separate soil material. Initial concentration of Br was set to zero; initial NO<sub>3</sub> concentrations were selected as presented below.

To calibrate the model: (1) flux-averaged concentrations across the nine outlets for each row were used to compare simulated and measured values; (2) hydraulic properties of the layers were initially set equal to the HYDRUS-2D defaults for the textural classes of the layers as listed in Table 1; (3) the saturated hydraulic conductivity was calibrated; (4) longitudinal and transverse dispersivities were then allowed to vary in calibrations with Br data by using the ‘inverse solution’ option of the software; (5) the first-order denitrification rates were allowed to vary in calibrations with NO<sub>3</sub> data.

The saturated hydraulic conductivity was calibrated manually; the HYDRUS-2D ‘inverse solution’ option could not be used because this option in HYDRUS-2D does not support two different types time-variable boundary conditions that were simultaneously present in our simulation scenarios. The sum of squared differences between observed and simulated outflow data from Rows 2, 3, and 4 was minimized. First set was ignored and the ‘inverse solution’ option of HYDRUS-2D was used to find the initial estimates of  $K_s$  in three layers; those estimates were 150, 25, and 17 cm d<sup>-1</sup>. These initial esti-

mates were used to establish ranges in which  $K_s$  should be searched. One hundred-twenty five runs of the code were performed in which  $K_s$  in the layer 0 to 25 cm varied from 140 to 180 cm d<sup>-1</sup> with a 10-cm d<sup>-1</sup> increment; the 25- to 35-cm layer varied from 20 to 40 cm d<sup>-1</sup> with a 5-cm d<sup>-1</sup> increment; and the 35- to 45-cm layer varied from 10 to 30 cm d<sup>-1</sup> with a 5-cm d<sup>-1</sup> increment.

Flux-averaged concentrations  $\bar{c}_j$  were computed as

$$\bar{c}_j = \frac{\sum_{i=1}^N c_{ij} q_{ij}}{\sum_{i=1}^N q_{ij}}$$

where  $j$  is the row number,  $i$  is the number of an individual outlet in a row,  $i = 1, 2, \dots, N$ ,  $N$  is the total number of outlets in a row ( $N = 9$  in this work),  $c_{ij}$  and  $q_{ij}$  are the concentration and the water flux observed in the  $i$ th outlet of the  $j$ th row, respectively. Computations of  $\bar{c}_j$  were performed separately for each observation time.

## RESULTS AND DISCUSSION

### Experimental Data

Figure 2 shows Br and NO<sub>3</sub> distribution patterns across the nine outlets of the top three active outlet rows (at 20-, 30-, and 40-cm soil depths). The lack of early breakthroughs from outlet Numbers 1 and 9 indicates little if any preferential flow along the chamber walls (i.e., next to the gravel-filled chambers). The general rapid rise at the leading edge of the BTCs near Day 2 followed by an asymmetrical decreasing BTC, however, is characteristic of preferential flow, most likely through the larger pore sequences within the undisturbed soil monolith. Increasing temporal asymmetries around the peak concentrations with increasing soil depth suggests a simultaneous and gradual decrease in preferential flow and an increase in lateral dispersion processes within the soil profile.

The summary of experimental data averaged across outlet rows is shown in Fig. 3. The second, third, and fourth outlet rows generated nearly 100% of the outflow (Fig. 3a). The flow from the second row was about two times greater than from the third row. In spite of constant inlet and outlet water-heads, head-gradient, and influent ionic strength, temporal variability in the outflow was quite large. All nine outlets of the second row generated effluent during the transport experiment (Fig. 3c), whereas the number of working outlets in Rows 3 and 4 varied with time. Two to three outlets in Row 3, and two to four outlets in Row 4 did not have flow during the experiment. There was just a single outlet in the fifth row that generated intermittent very low flow. There was a general trend of increasing flow rates during the experiment in rows 2 to 4 (Fig. 3a), which could be related to the presence of some entrapped air in the beginning of the experiment. Other dynamic factors that could influence flow rates include: increased biological activity due to NO<sub>3</sub> tracer influx, for example, N<sub>2</sub> and N<sub>2</sub>O production from denitrification; root growth and respiration; and the introduction of K in the system with the Br and NO<sub>3</sub> tracer solution might have had some minimal effect on soil structure and water flow.

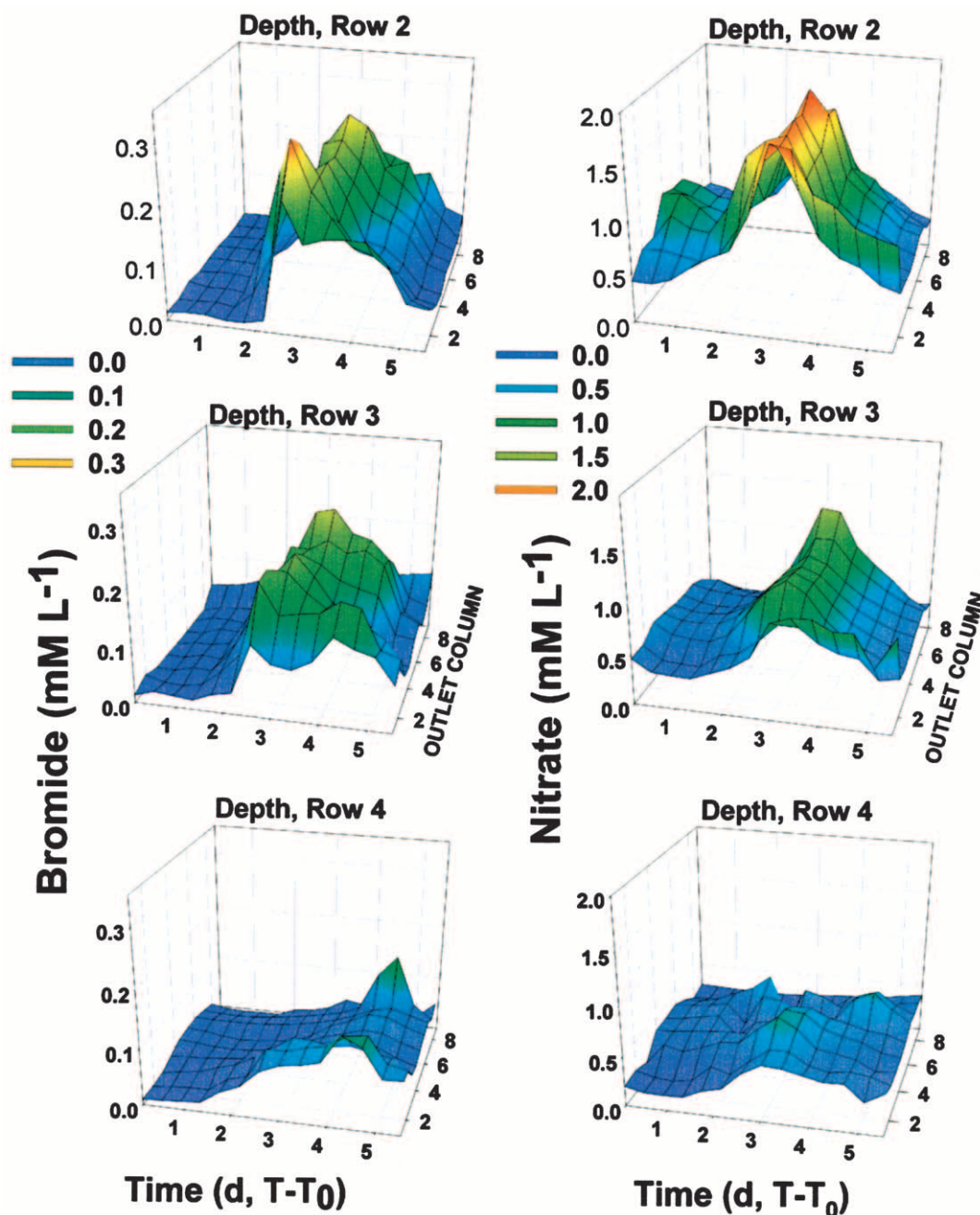


Fig. 2. Bromide and  $\text{NO}_3$  breakthrough curves across nine outlet ports at three outlet rows.

The standard deviations of flow rates across rows were similar among rows (Fig. 3b), making the flow rate coefficients of variation (CV) inversely proportional to the flow rates. There was a slight increase in standard deviations of flow rates along with the increase of the flow rates (Fig. 3a and 3b).

Bromide BTCs were similar in Rows 2 and 3 (Fig. 3d) in spite of the large differences in flow rates between rows (Fig. 3a). The variability of the Br BTC increased as the BTC reached peak concentrations, then became relatively stable (Fig. 3e). The ratio of flux-averaged Br concentration to the mean concentrations (Fig. 3d and 3f) varied from 0.84 to 1.06 in the top sandy loam layer, from 0.72 to 1.04 in the loam layer, and from 0.78 to

1.16 in the sandy clay loam layer, suggesting that the flow paths with largest fluxes carried relatively smaller solute concentrations. The  $\text{NO}_3$  breakthrough, shown in Fig. 3g through 3i, in contrast to the Br breakthrough, was smaller in Row 3 than in Row 2. Note, that the initial  $\text{NO}_3$  concentration in the BTC was much higher in Row 2 than in Row 3.

Normalized flux-averaged breakthrough concentrations of Br and  $\text{NO}_3$  are compared in Fig. 4. The BTCs of  $\text{NO}_3$  and Br were similar while the concentrations rose, then became distinctly different. The Br and  $\text{NO}_3$  increasingly diverged in the tail of the BTC, with the  $\text{NO}_3$  BTC concentration in Row 2 becoming less than the original concentration by the end of the observa-

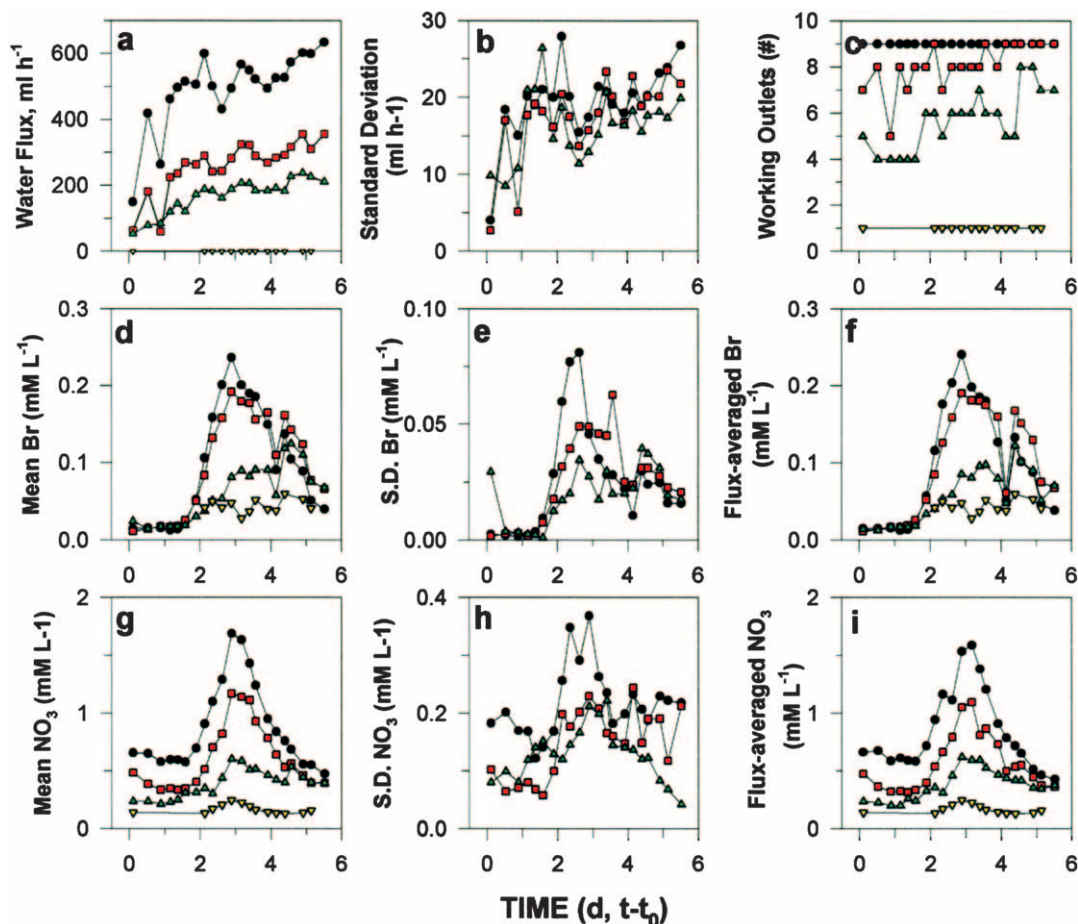


Fig. 3. Experimental data on flow and transport: (a) total water fluxes at the outlet rows, (b) variability (standard deviation) in water fluxes among individual outlet ports, (c) number of flowing individual outlet ports, (d) mean Br concentrations by row, (e) standard deviation in Br concentrations by row, (f) flux-averaged Br concentrations by row, (g) mean  $\text{NO}_3$  concentrations by row, (h) standard deviation in  $\text{NO}_3$  concentrations by row, (i) flux-averaged  $\text{NO}_3$  concentrations for the outlet rows. Symbols: ● = Row 2, ■ = Row 3, ▲ = Row 4, ▼ = Row 5.

tions. This divergence in BTCs as well as the relative concentration in Row 2 becoming negative is likely due primarily to denitrification under these near-saturated conditions.

Effluent mass balances for Br,  $\text{NO}_3$ , and water flux data are shown in Table 2. The bulk of the flow (>99%) occurred in Rows 2 to 4 and logarithmically decreased ( $r^2 > 0.98$ ) with soil depth. Overall, 87% of the Br was

accounted for in the chamber effluent. Visual analysis of Fig. 4 shows that some of the unaccounted for Br remained in the soil, as the breakthrough concentrations of Br were substantial at the end of the observation period. The  $\text{NO}_3$  data are more complex, with 40% accounted for in the effluent, but very little apparently left in the soil monolith (Fig. 4), with final breakthrough concentrations being smaller than the initial values. The

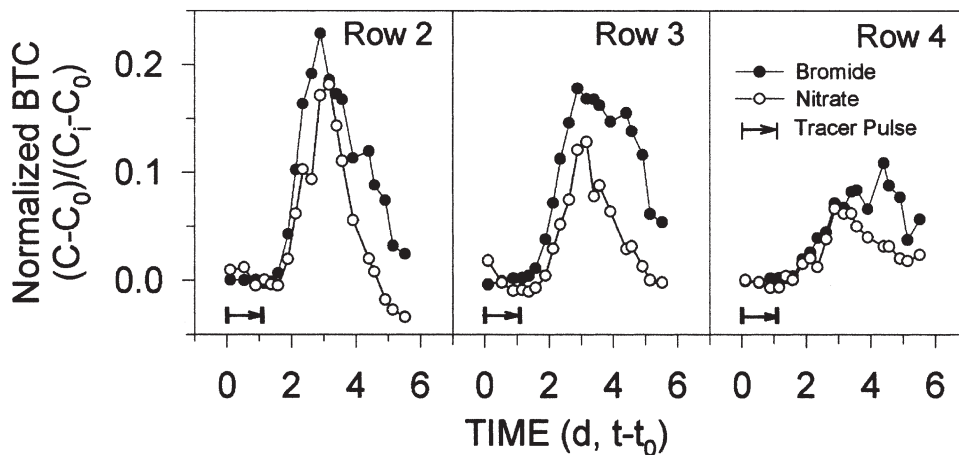


Fig. 4. Normalized flux-averaged Br and  $\text{NO}_3$  breakthrough concentrations.



**Table 2. Tracer mass balance components, and measured vs. fitted mean water flux densities.**

Outflow rows	Tracers		Mean water flux	
	Br	NO <sub>3</sub>	Measured†	Fitted
	mM		mL h <sup>-1</sup>	
			Outflow	
2	5.47	15.61	523 ± 47	540
3	3.13	7.20	282 ± 36	302
4	1.13	3.93	181 ± 35	188
5	0.06	0.03	—	10
Total outflow	9.79	26.77		
	Inflow			
Total inflow	11.26	67.58		

† Water flux means across Days 1 through 5.5, ±1 standard deviation.

loss of NO<sub>3</sub> must be primarily due to denitrification and plant uptake. In the absence of plant uptake data and the near-saturated conditions, we are assuming that the primary loss mechanism is by denitrification.

Based on the relative changes in Br and NO<sub>3</sub> concentrations at the tails of the BTCs (see Fig. 3 and 4), about 60% of the supplied NO<sub>3</sub> was denitrified in the system. In contrast to the influent NO<sub>3</sub> to Br millimolar ratio of 6.0, the effluent millimolar ratios were 2.8, 2.3, and 3.5 in outlet Rows 2, 3, and 4. This indicated that NO<sub>3</sub> losses, characterized here as denitrification, was more active in the upper layers of the profile, in spite of a much lower flow velocity in the deeper layers (Fig. 3a) and therefore, much longer residence time of the NO<sub>3</sub> in the deeper layers. It is postulated that the greater NO<sub>3</sub> loss in Row 3 may be due to the longer O<sub>2</sub> path length to Row 3 than to Row 2 (i.e., more anaerobic), and to more organic C (as an energy source for denitrification) compared with that in the Bt horizon below (Row 4).

### Solute Transport Modeling

The HYDRUS-2D model was calibrated first to estimate hydraulic conductivity values for the first three layers, using the data from the outlet water fluxes. The simulated average transpiration rate was 86 mL h<sup>-1</sup> and constituted about 8.7% of the flow rate from the outlet ports. The HYDRUS-2D model was then used to fit the solute transport to the Br data. Both ADE and MIM models were tested. Longitudinal  $D_L$  and transversal  $D_T$  dispersivities were included in the list of calibrated parameters for the first three layers. Longitudinal dispersivities for the bottom clay loam layer and the two sandy endplates were set to typical values (Table 3) for those textures and scale (Perfect et al., 2002). Varying those

values by a half-order of magnitude, however, changed the simulation results by <5% (data not shown); probably because the clay loam layer and sandy endplates had extremely slow and fast flows, respectively. It is to be noted that the transversal dispersivities were set one order of magnitude lower than longitudinal in those layers. The MIM model gave a slightly better fit to the data indicating the presence of dual porosity in the first two layers. The determination coefficients  $R^2$  of the regressions of predicted vs. observed values were equal to 0.842 and 0.873 for the ADE and MIM models, respectively. However, the water content in the immobile zone and the rate constant for the mass exchange between the two zones were strongly negatively correlated, suggesting that the MIM was over-parameterized for this data set. Therefore, the ADE was used as a Br transport model.

Fitted Br flow and transport parameters are shown in Table 3, and corresponding simulated Br BTCs are shown in Fig. 5. The magnitude of the dispersivity values is typical of values for the field scale soil column (Zhang et al., 1994). Estimated longitudinal dispersivities decreased with depth whereas the transversal dispersivities increased with depth. The standard error of the parameter estimates decreased with depth, possibly due to higher variability in flux and concentrations of the outlet data from the fourth row. The increase in transversal mixing with depth could provide better conditions for denitrification than in the top layer.

A snapshot of the simulated water flow velocity distribution (Fig. 6) shows that the small diameter inlet and outlet ports created strong focused flows near the inlet and outlet walls. This HYDRUS-2D simulation shows that part of the flow in the top sandy loam layer was diverted to pass through the outlets in the loamy layer (Row 3). The relatively high BTC for Row 3 (Fig. 3), despite a much lower hydraulic conductivity value compared with Row 2 (Table 3), may be the result of a sudden change in flux direction from Row 2 to 3, as indicated by the convergence of flow vectors near the outlet in Fig. 6.

HYDRUS-2D Br-tracer simulations within the soil block (spectral map with isolines) are shown in Fig. 7 at four selected times following the start of the 1.08-d tracer pulse. The tracer distribution at 0.50-d shows the impact of: (i) the inlet head with very little influx above 10 cm (Row 1) and (ii) the proportionately high conductivity of the sandy loam layer (0–25 cm). The simula-

**Table 3. Flow and transport parameters† used to simulate Br transport.**

Layer‡	$\theta_s$	$\theta_r$	$\alpha$	$n$	$K_b$	$D_L$ §	$D_T$ §
	cm <sup>3</sup> cm <sup>-3</sup>				cm d <sup>-1</sup>	cm	
1 SL	0.41	0.065	0.075	1.89	170	10.0 ± 2.00	2.1 ± 2.03
2 L	0.39	0.078	0.036	1.56	30	7.6 ± 7.6	3.3 ± 4.02
3 SCL	0.37	0.100	0.059	1.48	15	10.1 ± 111.5	15.9 ± 84.8
4 CL	0.41	0.095	0.019	1.31	2.2	10.0	1.0
5 end-plates	0.43	0.045	0.145	2.68	712.8	1.0	0.1

†  $\theta_s$  is the saturated water content,  $\theta_r$  is the residual water content,  $\alpha$  and  $n$  are shape parameters in van Genuchten's equation for water retention,  $\theta_s$ ,  $\theta_r$ ,  $\alpha$ ,  $n$  were estimated using the Rosetta software;  $K_b$  is the saturated hydraulic conductivity,  $D_L$  is the longitudinal dispersivity,  $D_T$  is the transversal dispersivity.

‡ Four textural layers shown in Table 1 and Fig. 1, and the sand end-plates at the inlet and outlet face of the in situ chamber.

§ Optimized value ± standard error.

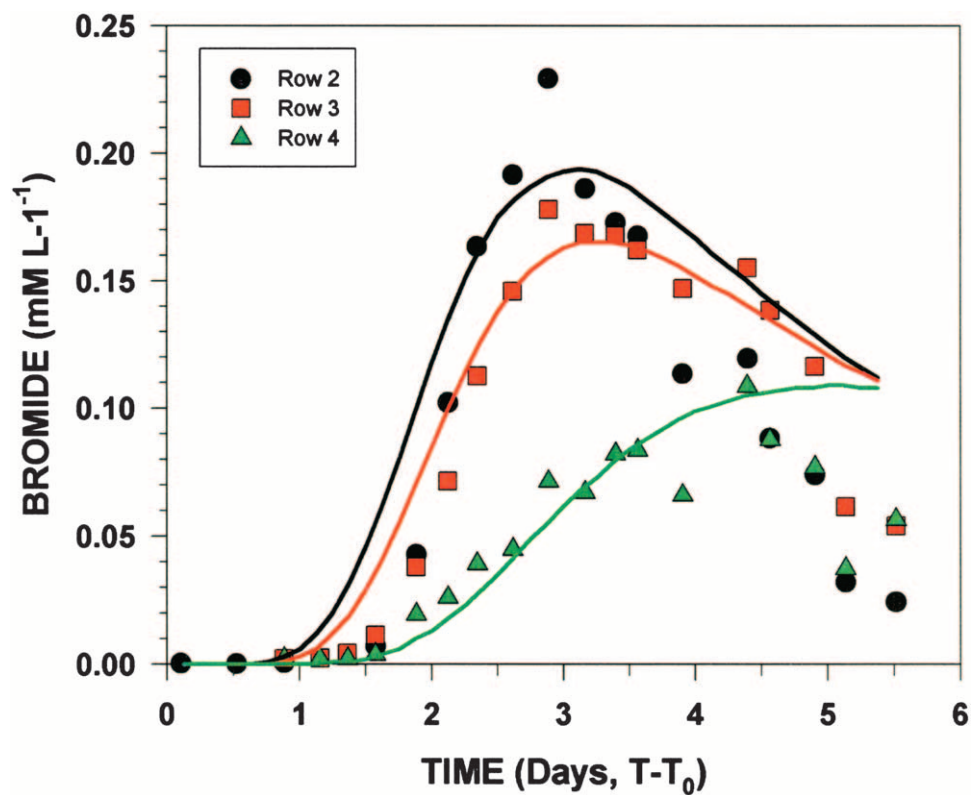


Fig. 5. Measured (symbols) and simulated (lines) flux-averaged Br breakthrough by row.

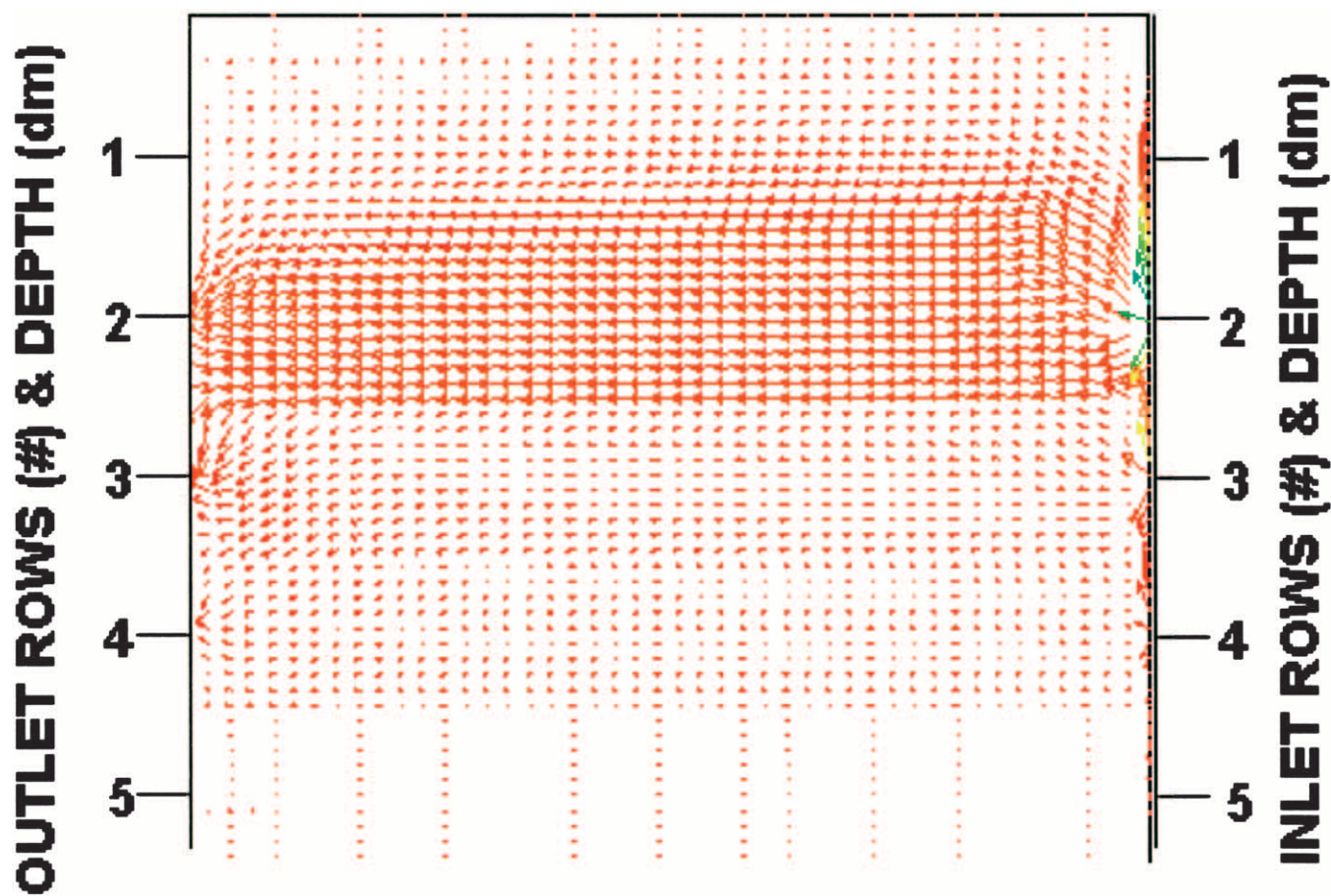


Fig. 6. HYDRUS-2D analysis vector-plot of flow velocities within the soil monolith.



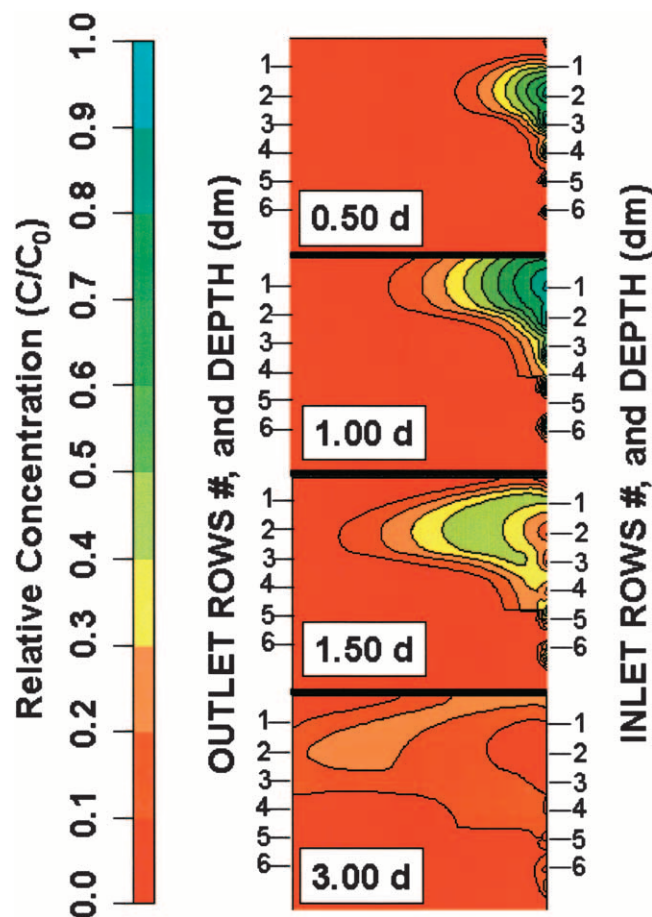


Fig. 7. HYDRUS-2D Br lateral transport simulations within the soil monolith at four times after the initiation of the 1.08-d Br-tracer pulse.

tions suggest that the high conductivity of the inlet sand plate enabled tracer input to the entire inlet face but resulting in very little movement into the sandy clay loam layer. All four time panels show the primary transport occurring within the sandy loam layer. The peak BTC came at about Day 3.0 (Fig. 3–5) with tailing concentrations that did not return to zero by the end of 5.5 d. Some of the causes for the long tail can be postulated from the spectral map at 3.0 d that shows diluted Br spread across most of the 0.9-m wide soil block. There appears to be a significant time lag on the tracer flow at the interfaces between the zones of lower and higher hydraulic conductivity regions. That is, near the interface of the unsaturated and saturated regions above the inlet and outlet heads, and at the interface between the sandy loam and loam layers at about 25 cm.

To simulate the  $\text{NO}_3$  transport, the initial  $\text{NO}_3$  concentrations were assumed to be constant across each of the soil layers. Those values were adjusted manually to provide the initial concentrations at the outlets being approximately the same as the observed resident concentrations, that is, 0.7, 0.35 and 0.19  $\text{mM NO}_3 \text{ L}^{-1}$  for the layers 1, 2, and 3 to 4, respectively. The Br dispersion parameters were used to simulate  $\text{NO}_3$  transport. The first order removal  $\text{NO}_3$  from solution due to denitrification was assumed. The  $\text{NO}_3$  transport was, in general,

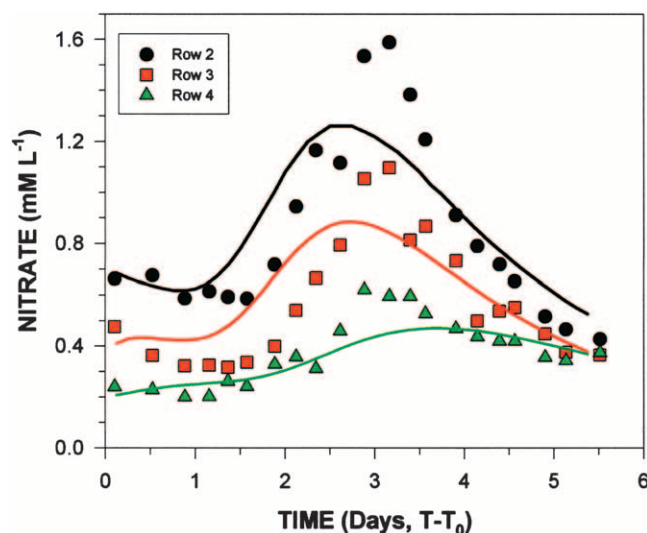


Fig. 8. Measured and simulated flux-averaged  $\text{NO}_3$  breakthrough concentrations.

simulated well (Fig. 8) with a relatively high regression coefficient ( $R^2 = 0.828$  of the regression of simulated vs. measured values). Values of  $R^2$  were smaller when computed for each specific outlet row, and varied from 0.711 to 0.761. Simulated grass nitrate uptake was about 0.9% of the nitrate influx through the inlets. Inspection of this figure shows that the simulated increase in  $\text{NO}_3$  concentrations at the outlets occurred somewhat earlier as compared with the measured one. The calibrated values of the denitrification rates were  $0.020 \pm 0.028 \text{ d}^{-1}$ ,  $0.713 \pm 0.211 \text{ d}^{-1}$ , and  $0.010 \pm 0.185 \text{ d}^{-1}$  (rate  $\pm$  standard error) in the sandy loam Layer 1, the loam Layer 2, and silty clay loam Layer 3, respectively. These first-order denitrification rates fall within the rate range from 0.02 to  $8.0 \text{ h}^{-1}$  obtained by Sheibley et al. (2003) for sediment perfusion cores.

## CONCLUSIONS

The in situ chamber for studying lateral flow under shallow water table and riparian zone conditions provided an effective experimental setup to study a predominately horizontal flow regime with a prescribed hydraulic gradient. It allowed for detailed observations of reaction and transport that can be useful for understanding and interpreting the effect of the fine-scale heterogeneity on the outcomes of the coarser scale modeling performed at field and watershed levels. The field test that was completed herein provided information about the chamber functioning that can be used for comparison of the chamber with other types of setups to study lateral flow and transport, for example, slotted wells. The lack of steady flow and the convergence of flow due to outlet configuration may require more sophisticated models to interpret the results. However, overall, the HYDRUS-2D model provided good results in simulating flow and transport processes in the soil monolith. Simulations also provided valuable insights in the details of the transport inside the chamber. The chamber represents the minimum

experimental scale at which transport and biologic transformation occur similar to the real world.

### ACKNOWLEDGMENTS

The authors are grateful to Peter Downey, Support Scientist at USDA-ARS, for invaluable field assistance and technical support.

### REFERENCES

- Angier, J.T., G.W. McCarty, C.P. Rice, and K. Bialek. 2002. Influence of a Riparian Wetland on nitrate and herbicides exported from an agricultural field. *J. Agric. Food Chem.* 50:4424–4429.
- Bosch, D.D., J.M. Sheridan, and R.R. Lowrance. 1996. Hydraulic gradients and flow rates of a shallow coastal plain aquifer in a forested riparian buffer. *Trans. ASAE* 39:865–871.
- Bragan, R., J.L. Starr, and T.B. Parkin. 1997. Shallow groundwater denitrification rate measurement by acetylene block. *J. Environ. Qual.* 26:1531–1538.
- Day, R.L., A.M. Calmon, J.M. Stiteler, J.D. Jabro, and R.L. Cunningham. 1998. Water balance and flow patterns in a fragipan using in situ soil block. *Soil Sci.* 163:517–528.
- Gilliam, J.W. 1994. Riparian wetlands and water quality. *J. Environ. Qual.* 23:896–900.
- Hamilton, P.A., J.M. Denver, P.J. Phillips, and R.J. Shedlock. 1993. Water-quality assessment of the Delmarva Peninsula, Delaware, Maryland, and Virginia—Effects of agricultural activities on, and distribution of nitrate and other inorganic constituents in the surficial aquifer. U.S. Geol. Surv. Open file Rep., 93–40. U.S. Gov. Print. Office, Washington, DC.
- Hargreaves, G.H., and Z.A. Samani. 1985. Reference crop evapotranspiration from temperature. *Appl. Eng. Agric.* 1:96–99.
- Jordan, T.E., D.L. Correll, and D.E. Weller. 1993. Nutrient interception by a riparian forest receiving inputs from adjacent cropland. *J. Environ. Qual.* 22:467–473.
- Lowrance, R., L.S. Altier, R.G. Williams, S.P. Inamdar, J.M. Sheridan, D.D. Bosch, R.K. Hubbard, and D.L. Thomas. 2000. REMM: The Riparian Ecosystem Management Model. *J. Soil Water Conserv.* 55:27–34.
- Maitre, V., A.-C. Cosandey, E. Desagher, and A. Parriaux. 2003. Effectiveness of groundwater nitrate removal in a river riparian area: The importance of hydrogeological conditions. *J. Hydrol. (Amsterdam)* 278:76–93.
- Mendoza, G., and T.S. Steenhuis. 2002. Determination of hydraulic behavior of hillsides with a hillslope infiltrometer. *Soil Sci. Soc. Am. J.* 66:1501–1504.
- Muñoz-Carpena, R., J.E. Parsons, and J.W. Gilliam. 1999. Modeling hydrology and sediment transport in vegetative filter strips. *J. Hydrol. (Amsterdam)* 214:111–129.
- Parkin, T.B., E.E. Codling, J.J. Meisinger, and J.L. Starr. 1988. Variability of groundwater nitrate concentrations in non-agricultural ecosystems. p. 272–282. *In* Understanding the estuary: Advances in Chesapeake Bay research. Proceedings of a Conference. 29–31 Mar. 1988. Baltimore, MD. Chesapeake Research Consortium Pub. 129. Chesapeake Research Consortium, Edgewater, MD.
- Perfect, E., M.C. Sukop, and G.R. Haszler. 2002. Prediction of dispersivity for undisturbed soil columns from water retention parameters. *Soil Sci. Soc. Am. J.* 66:696–701.
- Reynolds, W.D., and D.E. Elrick. 1985. *In situ* measurement of field-saturated hydraulic conductivity, sorptivity, and the  $\alpha$ -parameter using the guelph permeameter. *Soil Sci.* 140:292–302.
- Sadeghi, A.M., and J.L. Starr. 1992. Transport in a horizontal flow chamber. *Soil Sci. Soc. Am. J.* 56:600–603.
- Sheibley, R.W., A.P. Jackman, J.H. Duff, and F.J. Trisk. 2003. Numerical modeling of coupled nitrification–denitrification in sediment perfusion cores from the hyporheic zone of the Shingobee River, MN. *Adv. Water Res.* 26:977–987.
- Simunek, J., M. Sejna, and M.Th. van Genuchten. 1999. The HYDRUS-2D software package for simulating two-dimensional movement of water, heat, and multiple solutes in variably saturated media. Version 2.0, IGWMC-TPS-53. International Ground Water Modeling Center, Colorado School of Mines, Golden.
- Starr, J.L., A. Sadeghi, T.B. Parkin, and J.J. Meisinger. 1996. A tracer test to determine the fate of nitrate in shallow ground water of riparian zones. *J. Environ. Qual.* 25:917–923.
- Timlin, D.J., Y. Pachepsky, B.A. Acock, J. Simunek, G. Flerchinger, and F.D. Whisler. 2002. Error analysis of soil temperature simulations using measured and estimated hourly weather data with 2DSOIL. *Agric. Syst.* 72:215–239.
- Van Genuchten, M.Th. 1980. A closed-form equation for predicting the hydraulic conductivity of unsaturated soils. *Soil Sci. Soc. Am. J.* 44:892–898.
- Vellidis, G., R. Lowrance, P. Gay, and R.K. Hubbard. 2003. Nutrient Transport in a Restored Riparian Wetland. *J. Environ. Qual.* 32:711–726.
- Zhang, R., K. Huang, and J. Xiang. 1994. Solute movement through homogeneous and heterogeneous soil columns. *Adv. Water Res.* 17:317–324.